

## Mechanical behavior and crack tip plasticity of a strain aging sensitive steel

J. Belotteau<sup>a,c</sup>, C. Berdin<sup>a,\*</sup>, S. Forest<sup>b</sup>, A. Parrot<sup>c</sup>, C. Prioul<sup>a</sup>

<sup>a</sup> L.MSSMat, Ecole Centrale Paris, CNRS/UMR8579, Gde voie des Vignes, 92295 Châtenay Malabry Cedex, France

<sup>b</sup> MINES ParisTech, Centre des Matériaux, CNRS UMR7633, BP 87, 91003 Evry Cedex, France

<sup>c</sup> EDF R&D/MMC, Site des Renardières, 77818 Moret s/Loing Cedex, France

### ARTICLE INFO

#### Article history:

Received 12 November 2008

Received in revised form 8 July 2009

Accepted 10 July 2009

#### Keywords:

Strain aging

Crack tip plasticity

Fracture toughness

Viscoplastic material behavior

Finite element modeling

### ABSTRACT

C–Mn steels are prone to static and dynamic strain aging (SSA and DSA) that induce Lüders or Portevin–Le Chatelier strain localization phenomena. Tensile tests and fracture tests were carried out between 20 °C and 350 °C. Negative strain rate sensitivity (SRS) and discontinuous yielding were evidenced, in relation with a drop in fracture toughness. The Kubin–Estrin–McCormick (KEMC) constitutive law, well suited for this kind of material response, was identified so as to model the mechanical behavior of the ferritic steel from 20 °C up to 350 °C. It is shown that both static and dynamic strain aging can be modeled by introducing a monotonic temperature dependence of all the parameters except the strain hardening parameter. Extra-hardening due to dynamic strain aging is clearly evidenced. The influence of SSA and DSA on the plastic zone development at the crack tip of CT specimens is analyzed on the basis of a finite element study.

© 2009 Elsevier B.V. All rights reserved.

### 1. Introduction

Many structural materials are prone to strain aging, which causes inhomogeneous yielding such as Lüders bands and Portevin–Le Chatelier (PLC) instabilities. These phenomena are related to strain or strain rate localization and occur for different temperature and strain rate ranges. Dynamic strain aging is related to inverse strain rate sensitivity and induces a jerky flow when the strain rate sensitivity becomes negative [1]. Strain aging is generally associated with a significant drop in both ductility and ductile tearing resistance in ferritic steels [2,3]. Nevertheless, some authors have found an inverse effect of strain aging on fracture toughness when testing pure iron or other metals [4,5]. Hence, the influence of strain aging on fracture toughness remains controversial.

Strain aging occurs in steels containing interstitial elements in solid solution such as carbon or nitrogen, which segregate to dislocations thus inducing dislocation pinning [6]. Several models of the Lüders or PLC phenomena can be found in the literature. The first class of models is based on classical elastic-viscoplastic model with von Mises plasticity; as suggested by Tsukahara and Jung [7] the numerical simulation of the Lüders band is made possible by introducing a phenomenological local softening behavior at the beginning of plastic flow, followed by a classical strain harden-

ing law. In the same way, Benallal et al. [8] have modeled the PLC bands in smooth and notched specimens, using a piecewise linear stress–strain rate function that reproduces the negative strain rate sensitivity.

The second class of models takes into account the physical origin of strain aging, i.e., the pinning of dislocations by solute atmospheres that diffuse during straining, by means of an internal variable called the aging time [9]. This constitutive model was implemented in finite element codes in Refs. [10,11], thus allowing the simulation of both Lüders and Portevin–Le Chatelier (PLC) instabilities, by choosing the appropriate set of parameters [12]. Nevertheless, till now, this model has not been identified in order to predict both static and dynamic strain aging in the whole range of temperatures and strain rates that are relevant for steels. Such an extended identification is for example required to predict the fracture toughness (or any other mechanical properties) dependence on temperature in strain aging sensitive steels.

Ferritic steels such as C–Mn steels used for structural components in power plants (feedwater line and steam line of pressurized water nuclear reactors) are sensitive to dynamic strain aging at in-service temperatures [13–15]. Consequently, the fail-safe design of the component requires the prediction of the fracture toughness of the material in the presence of strain aging. With a view to account for strain aging in the mechanics of ductile fracture and to predict the specific temperature dependence of the fracture toughness, it is necessary to correctly compute the mechanical fields ahead of the crack tip. So, in the first step, this work aims at predicting the mechanical behavior of ferritic steel in the temperature range of

\* Corresponding author. Tel.: +33 1 41 13 13 25; fax: +33 1 41 13 14 30.

E-mail addresses: [jeanne.belotteau@ecp.fr](mailto:jeanne.belotteau@ecp.fr) (J. Belotteau), [clotilde.berdin@ecp.fr](mailto:clotilde.berdin@ecp.fr) (C. Berdin), [samuel.forest@ensmp.fr](mailto:samuel.forest@ensmp.fr) (S. Forest), [aurore.parrot@edf.fr](mailto:aurore.parrot@edf.fr) (A. Parrot), [claud.prioul@ecp.fr](mailto:claud.prioul@ecp.fr) (C. Prioul).

20–350 °C where SSA and DSA occur. The mechanical fields are then computed in cracked specimens.

The first part is devoted to the presentation of the experimental database that we obtained for the C–Mn steel studied in this work: tensile tests were performed in a large temperature range for two strain rates. The resistance to ductile tearing was also measured from 20 °C to 350 °C. In the second part, the Kubin–Estrin–McCormick (KEMC) constitutive model is introduced. The parameters of this model are identified over the entire temperature range, using the experimental database obtained in tension, together with information from literature. The identification procedure combines volume element simulation of material response and full-field simulations. Finite element modeling of tensile tests is required in order to predict strain and strain rate localizations. The mechanical behavior identified in such a way is then used to predict the mechanical fields in a CT specimen. The influence of strain aging on the development of the plastic zone at the crack tip is investigated and the local stress and strain fields are compared with those obtained by using a classical behavior law. Finally, some difficulties encountered to identify the model parameters over the entire temperature range are discussed leading to few proposals to improve the identification procedure and the predictive capabilities of the KEMC model.

## 2. Experimental procedure

### 2.1. Material

The steel used in this study is a C–Mn steel containing (in wt%) 0.19 C, 0.0074 S, 0.011 P, 0.27 Si, 1.07 Mn, 0.04 Ni, 0.01 Mo, 0.05 Cu, 0.011 N, and 0.0085 Al. This material, called TU48C in the following, is very sensitive to strain aging due to the small Al content.

The material is extracted from a seamless secondary coolant pipe obtained by a circular rolling process. The microstructure is composed of ferrite and pearlite in alternate bands along planes parallel to the axial and circumferential directions. The crystallographic texture was not analyzed. However, the section of the cylindrical tensile specimen remains circular up to fracture strain. So, the mechanical behavior is isotropic at least in the long and short transverse plane. By extension we considered the mechanical behavior as fully isotropic, weakly affected by the morphological texture, nor by a crystallographic texture.

### 2.2. Tensile tests

Tensile tests were performed in order to characterize the TU48C C–Mn steel in the temperature range where SSA and DSA phenomena occur. Cylindrical tensile specimens with 36 mm gauge length and 6 mm diameter were tested. A 500 kN tensile test machine, equipped with a halogen lamp heater furnace, was used. The temperature regulation was controlled by a thermocouple welded on the sample, and strain measurements were made with an extensometer placed on the gauge length of the sample. The experiments were conducted at the imposed crosshead displacement speed computed in order to maintain the prescribed strain rate in the plastic part of the curve. Tensile tests were carried out at seven temperatures between 20 °C and 350 °C and at two constant strain rates:  $10^{-2} \text{ s}^{-1}$  and  $10^{-4} \text{ s}^{-1}$  thus giving access to the temperature dependence of the strain rate sensitivity of the material.

Lüders peak and plateau, associated with static strain aging, were observed from 20 °C to 200 °C. The peak can be interpreted as the overstress necessary to unpin dislocations from their solute atmospheres [6]. Indeed, the so-called “microscopic yield stress” is defined by the intersection between the hardening curve extrapolated to zero plastic strain and the linear elastic part of the tensile

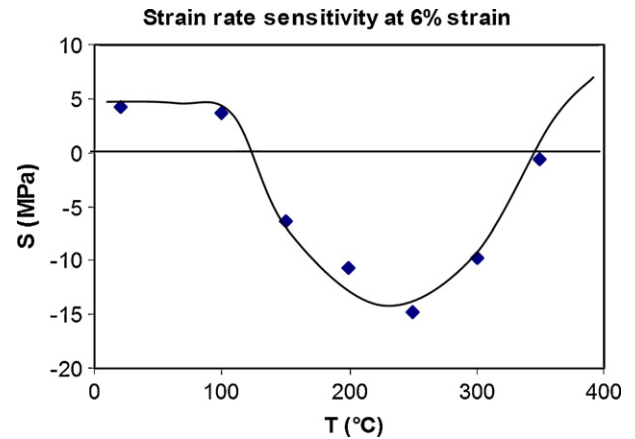


Fig. 1. Strain rate sensitivity measured at 6% strain as function of temperature for strain rates between  $10^{-2} \text{ s}^{-1}$  and  $10^{-4} \text{ s}^{-1}$ .

stress–strain curve. So, the overstress is the difference between the upper yield stress and this microscopic yield stress [6]. This overstress can be approximately estimated to 150 MPa at 20 °C (see Fig. 5). This value decreases with temperature and tends to zero for temperatures higher than 200 °C. It should be noted that the amplitude of the peak stress depends on the specimen geometry, especially on the fillet geometry between the specimen head and its gauge length [16]. Portevin–Le Chatelier instabilities were also observed from 150 °C to 300 °C, depending on the prescribed strain rate.

The strain rate sensitivity (SRS) coefficient  $S$  is defined as:

$$S = \frac{\sigma_2 - \sigma_1}{\ln \dot{\epsilon}_2 - \ln \dot{\epsilon}_1} \quad (1)$$

where  $\sigma_1$  and  $\sigma_2$  are the flow stresses at one given strain at the strain rates  $\dot{\epsilon}_1$  and  $\dot{\epsilon}_2$ , respectively. The coefficient  $S$  was measured at 6% strain for each tested temperature (Fig. 1). In contrast to the “usual” evolution of  $S$ , which would correspond to a monotonic increase with temperature, the reported values reveal a strain rate sensitivity drop due to DSA in the 100–400 °C temperature range. The 120–350 °C range corresponds to negative SRS values: these observations were correlated to the observation of PLC instabilities on the stress/strain curves. It is worth noting that the temperature domain for DSA is larger than the temperature domain of PLC [17]. The minimum value of the SRS coefficient is observed at 250 °C.

In agreement with previous tests made by Wagner et al. [14] in similar steels, DSA was also highlighted by non-classical evolutions of the tensile mechanical properties with temperature (Table 1): increase in ultimate tensile stress associated with a decrease in ductility.

### 2.3. Fracture tests

Another manifestation of DSA in steels is the decrease in fracture toughness observed in the same temperature range. In order to measure this property, tearing tests were performed between 20 °C and 350 °C on side-grooved compact tension (CT25) specimens according to 12135 AFNOR standard. The specimen geometry is 50 mm wide, 25 mm thick with a net thickness of 20 mm and an initial crack length  $a_0 = 30$  mm. The single-specimen unloading compliance method was applied: crack growth is estimated from specimen compliance measurement at partial unloading performed at various crack opening displacements. Following the normalization procedure, the calculation of the compliance is carried out assuming a straight crack front in a specimen loaded under plane strain. The tests were conducted at a prescribed crack opening displacement rate of 0.4 mm/min using a crack clip gauge. The

**Table 1**  
Mechanical properties of the C–Mn steel:  $R_{\text{inf}}$  is the lower yield stress (the flow stress of the Lüders plateau if existing),  $A_u$  is the uniform elongation before necking,  $R_m$  the ultimate tensile strength and  $J_{0.2}$  the initiation fracture toughness.

	$\dot{\varepsilon}$ (s <sup>-1</sup> )	20 °C	100 °C	150 °C	200 °C	250 °C	300 °C	350 °C
$R_{\text{inf}}$ (MPa)	10 <sup>-4</sup>	300	280	265	245	225	190	180
	10 <sup>-2</sup>	325	300	282	275	220	195	200
$A_u$ (%)	10 <sup>-4</sup>	23.5	18.7	16.2	13.4	16.1	17.4	15.6
	10 <sup>-2</sup>	22.3	19.3	17.5	15.3	13.7	14.5	18.7
$R_m$ (MPa)	10 <sup>-4</sup>	480	449	461	500	528	504	488
	10 <sup>-2</sup>	500	459	443	456	451	464	486
$J_{0.2}$ (kJ/m <sup>2</sup> )	–	269	311	169	178	167	258	366

initiation fracture toughness  $J_{0.2}$  (Table 1) and the ductile tearing modulus  $dJ/da$  were determined at the same temperatures as for tensile tests. A fracture test at 275 °C was added for an improved accuracy of the temperature dependence of the fracture toughness.

In agreement with previous results obtained by Wagner et al. [3] in similar steels, a drop in the tearing resistance between 100 °C and 300 °C, followed by an increase for higher temperatures is observed. Moreover, between 150 °C and 275 °C, the value of the initiation fracture toughness is about 50% lower than the fracture toughness measured at 100 °C and 300 °C. The same evolution is noted for the tearing modulus.

For tests performed in the 150–250 °C temperature range, the load versus crack opening displacement (COD) curves revealed serrations between each unloading period, before and during the tearing part of the curve (see Fig. 11). These serrations can be attributed to DSA effects. The tearing tests were also affected by static strain aging: for the tests performed in the 20–200 °C temperature range, the load versus COD curves present overload peaks at the end of each reloading step (see Fig. 11). Consequently, the drop in fracture properties mentioned above can unambiguously be associated with the occurrence of strain aging phenomena in the same temperature range.

### 3. Constitutive model for strain aging

The SSA and DSA phenomena result from the diffusion of solute atoms to dislocations temporarily arrested at obstacles such as forest dislocations [1]. The contribution of strain aging to the flow stress can be described by a constitutive model taking into account the time dependence of the pinning process, and introducing aging time kinetics [18]. In this study, we used the strain aging constitutive model proposed by Zhang et al. [11]. This model can describe both SSA and DSA plastic instabilities, depending on the values of the model parameters, as shown in Graff et al. [12].

The aging contribution is introduced in the yield function of an elastic-viscoplastic model by means of an additional internal variable. The stress is computed from the total strain  $\varepsilon$  and the plastic strain  $\varepsilon^p$ , through the Hooke's law, with  $\underline{\underline{C}}$  the elasticity tensor (Eq. (2)).

$$\sigma = \underline{\underline{C}}(\varepsilon - \varepsilon^p). \quad (2)$$

The plastic strain is computed from the normality law rule and the equivalent plastic strain rate  $\dot{p}$  follows a thermal activation law defined in Eq. (3).

$$\dot{\varepsilon}^p = \dot{p} \frac{\partial f}{\partial \sigma}; \quad \dot{p} = \dot{\varepsilon}_0 \exp\left(-\frac{E_a}{k_B T}\right) \sinh\left(\frac{V_a f(\sigma)}{k_B T}\right) \quad (3)$$

$$f = f \quad \text{if } f \geq 0 \quad \text{and} \quad f = 0 \quad \text{otherwise}$$

where  $T$  is the temperature in K,  $k_B$  is the Boltzmann constant and  $\dot{\varepsilon}_0$ ,  $E_a$ ,  $V_a$  are respectively a normalization strain rate, the activation energy and the activation volume of the physical mechanisms of

plasticity. The function  $f$  is the yield function which is based on a von Mises criterion with isotropic hardening:

$$f(\sigma) = J_2(\sigma) - R(p) - R_a(p, t_a), \quad (4)$$

$$\dot{R} = bQ(1 - bp) + H\dot{p}, \quad R(0) = R_0, \quad (5)$$

with  $J_2(\sigma)$  is the second invariant of the stress tensor deviator. The classical strain hardening is given by the term  $R(p)$  which follows the evolution law defined in Eq. (5); the parameters characterizing the evolution law of this variable are  $b$  that drives the cumulative equivalent plastic strain  $p$  at saturation of the exponential term,  $Q$  which is the corresponding hardening magnitude and  $H$  is the slope of a linear strain hardening term. The yield stress  $R_0$  is the “microscopic yield stress”, corresponding to the yield stress that would be measured in the same steel if all the mobile dislocations were unpinned. A second hardening term,  $R_a(p, t_a)$  is introduced in order to account for the strain aging hardening. It is assumed to be isotropic, and depends on the cumulative equivalent plastic strain  $p$ , but also on a new internal variable  $t_a$ , the aging time. The strain aging hardening is defined by:

$$R_a(p, t_a) = P_1 C_s(p, t_a), \quad \text{with} \quad C_s = 1 - \exp(-P_2 p^\alpha t_a^n) \quad (6)$$

$$\dot{t}_a = 1 - \frac{\dot{p}}{\omega} t_a, \quad t_a(t = 0) = t_{a0}. \quad (7)$$

The strain aging term  $R_a$  is proportional to the variable  $C_s$  that represents the saturated solute fraction for pinning of dislocations temporarily arrested by obstacles such as forest dislocations. This variable increases with the aging time  $t_a$  (a totally pinned state is given by  $C_s = 1$ ). The parameter  $P_1$  is related to the maximal additional stress for unpinning. The parameters  $P_2$  and  $\alpha$  drive the strain and time aging dependence of the pinning process. The parameter  $n$  is related to the pinning kinetics. Another parameter labeled  $\omega$  appears in the evolution law of the aging hardening. It is associated with the incremental strain resulting from the jump of unpinned dislocations from one obstacle to the next one. As shown by Eq. (6) the strain aging term follows an Avrami kinetics of “relaxation-saturation”. If the strain rate increases, the contribution of strain aging decreases and, consequently, a drop in flow stress is observed. This kinetics leads to a phenomenological simulation of the negative strain rate sensitivity responsible for plastic flow instabilities.

### 4. Identification of the temperature dependent parameters

#### 4.1. Identification procedure

The parameters are identified through the comparison between experimental and simulation. Classically, the experimental results are obtained on specimens in which the mechanical fields are homogeneous, so that the specimen can be considered as a volume element. Modeling the experiments just requires solving the system of differential equations defined in the previous section. Using a numerical solver of such differential equations, the simulation step is not time consuming. The identification procedure can therefore

be automated. So, we implemented the constitutive equations in a software [19], which provides a solver of differential equations with a 4th order Runge–Kutta method with automatic time stepping, and numerical optimization tools using the generalized least squared method. Parameters are identified so as to minimize the sum of the squared differences between experimental and simulated stress values at all recorded prescribed strain values for each tensile curve. Weighting factors are attributed to the various tensile tests depending on the number of recorded points.

However, the identification procedure of a strain aging model from experimental data significantly differs from the usual identification approach described above. This is due to the fact that some model parameters are related to the strain localization patterns that develop on the specimen surface and to the corresponding serrations on the overall tensile curve. Volume element simulations are therefore not sufficient for the identification. Full-field finite element simulations of the specimens are required. That is why the identification procedure applied in the present work is split into two main steps:

- step 1: volume element simulations are performed for the identification of the parameters governing the overall hardening and viscous behavior, independently of specific strain aging effects.
- step 2: finite element simulations on a plate tensile sample under plane stress conditions are performed for the identification of the parameters  $P_1$ ,  $P_2$  and  $\alpha$  that control the propagation of Lüders and/or PLC bands. The objective of the identification at this stage is to obtain a qualitative agreement of the type of serrations observed on the overall simulated and experimental load–displacement curves.

The simulation of time and spatial distributions of mechanical variables were performed with a finite element code including the KEMC model [12]. The two steps described above are then iterated to reach a better agreement between experiment and simulation. The first step can be automated in contrast to the second step due to the too long computation time of FE simulation with PLC instabilities. Such a procedure has already been successfully applied for an aluminum alloy in Ref. [20] and in a Nickel base superalloy in Ref. [21] but at a single temperature and in the absence of the Lüders phenomenon. The following subsection concentrates on the first step, describing the identification process for various temperatures. Section 4.3 reports in detail the finite element simulations corresponding to step 2, relative to the final results.

#### 4.2. Parameter identification

The constitutive equations presented above first depend on three parameters which are the classical viscoplastic parameters in the flow rule:  $\dot{\epsilon}_0$ ,  $E_a$ ,  $V_a$ . Four parameters then appear in the definition of the strain hardening:  $b$ ,  $Q$ ,  $H$  and  $R_0$ . The strain aging term still requires the introduction of six new parameters:  $P_1$ ,  $P_2$ ,  $\alpha$ ,  $n$ ,  $\omega$  and  $t_{a0}$ . Thus, the identification of 13 parameters at each temperature is needed for the modeling of the mechanical behavior of the material.

The viscoplastic parameters are easily identified by tensile tests at different strain rates in a range where dynamic strain aging does not occur. The value of activation energy is 0.0022 eV, which limits the influence of temperature in the athermal domain, as it should be. The value of  $\dot{\epsilon}_0$  is chosen in order to get always a positive strain rate sensitivity for the classical part of the behavior law (Table 2). The activation volume is identified at temperatures where dynamic strain aging is not active: at 20 °C, 100 °C and 350 °C. Strain rate and plastic strain rate are approximately equal, so the activation volume can be computed from the strain rate sensitivity coefficient

**Table 2**

Temperature independent parameters of the KEMC model.

$E_a$ (eV/at)	$\dot{\epsilon}_0$ (s <sup>-1</sup> )	$H$ (MPa)	$n$	$\omega$
$2.2 \times 10^{-3}$	$10^{-7}$	440	0.66	0.0015

$S$  defined by Eq. (1) and computed at 6% strain:

$$V_a = \frac{k_B T}{E_a} \frac{1}{S}. \quad (8)$$

The experimental results show that  $V_a$  varies linearly with temperature, so in the absence of dynamic strain aging,  $S$  is constant in this material in the temperature range under consideration.

At low temperature, static strain aging is only active at small plastic strains since dislocation unpinning is achieved at the end of the Lüders plateau. So, the strain hardening parameters are identified by fitting experiments and modeling only for plastic strains larger than the plateau strain. At higher temperatures, in the domain of solute drag, the flow stress is then a combination of classical strain hardening and hardening by strain aging pinning.

The parameter  $P_1$  controls the contribution of the pinning process on the flow stress. It can be interpreted as the interaction force between mobile dislocations and solute atoms. The amplitude of the Lüders peak stress is directly related to the value of  $P_1$ . As temperature increases, dynamic strain aging progressively occurs and the Lüders peak decreases and finally disappears, so that the  $P_1$  value must decrease with temperature. However, since the same hardening term accounts for both types of aging, the value of  $P_1$  also partly controls the amplitude of serrations in the PLC domain. Beyond this domain its value remains large to account for the dragging mode which induces the increase in  $R_m$  with temperature. The occurrence of the Lüders peak is determined by the value of the initial aging time,  $t_{a0}$ .

Some values of the parameters related to the description of strain aging are given in Ref. [22] for DSA at room temperature in aluminum alloys. In the present study, dedicated to C–Mn steel, DSA occurs at higher temperatures. Furthermore, the objective is to predict the fracture toughness properties at temperatures ranging from 20 °C up to 350 °C. Consequently, a temperature dependent set of parameters must be identified in order to account for the mechanical behavior of the steel over the whole temperature range.

The parameters were identified in the 20–350 °C temperature range in order to obtain the best fit of the experimental tensile test database. With a view to limiting the number of parameters to be identified at each temperature and for sake of simplicity, we chose to keep the following parameters independent of temperature:  $\omega$  and  $H$ . For aluminum alloys, the parameter  $n$  was chosen equal to 1/3 by Refs. [12,22]. Nevertheless, internal friction tests as those performed by Wagner et al. [13] on a similar C–Mn steel, showed that  $n$  is equal to 2/3 for these steels. The temperature dependence of the microscopic yield stress follows the same evolution as the Young's modulus as expected in the athermal region.

The parameters were independently identified at each temperature. However, we aimed at obtaining a monotonic evolution of parameters with temperature, as far as possible. The values of the temperature dependent parameters are given at 20 °C in Table 3. As usually observed in steels, the dislocation pinning by solute atoms at 20 °C is very strong. The evolutions of  $P_1$  and  $Q$  with temperature are reported in Fig. 2: for increasing temperatures,  $P_1$  decreases, whereas  $Q$  follows a non-monotonic evolution, with a

**Table 3**

Temperature dependent parameters of the KEMC model, values at 20 °C.

$R_0$ (MPa)	$Q$ (MPa)	$b$	$V_a$ ( $\times 10^{-30}$ m <sup>3</sup> )	$P_1$ (MPa)	$P_2$ (s <sup>-n</sup> )	$\alpha$
200	270	23	1527	120	$3 \times 10^{-4}$	0.1

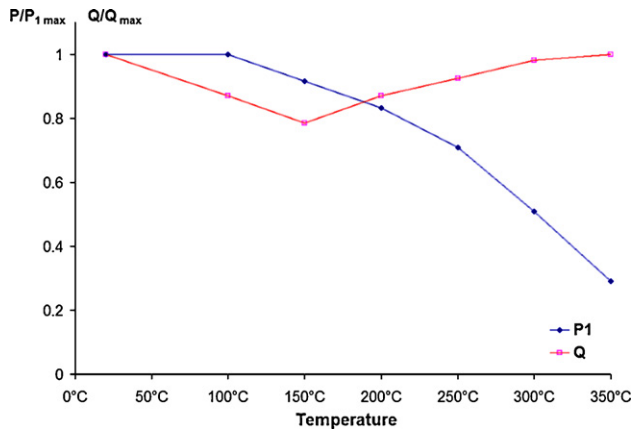


Fig. 2. Parameters  $P_1$  and  $Q$  as function of temperature.

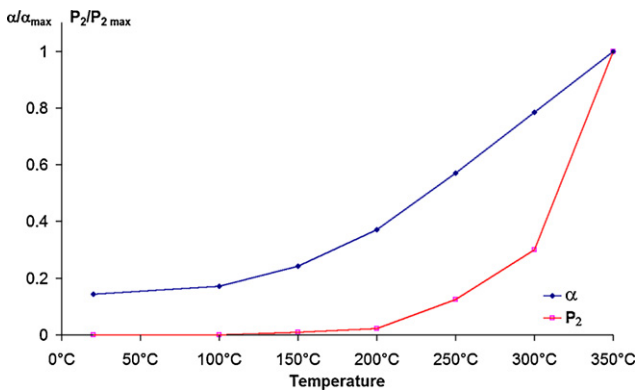


Fig. 3. Evolution with temperature of the parameters  $P_2$  and  $\alpha$  as function of temperature.

small drop and further quasi-constant level. The parameters  $P_2$  and  $\alpha$  are shown to increase with temperature (Fig. 3). The flow stress computed at 6% strain versus strain rate is reported in Fig. 4 for three temperatures. It increases with strain rate, this behavior corresponding to the classical viscosity of the material respectively for pinned dislocations (left side of the negative strain rate domain) and unpinned dislocations (right side of the negative strain rate

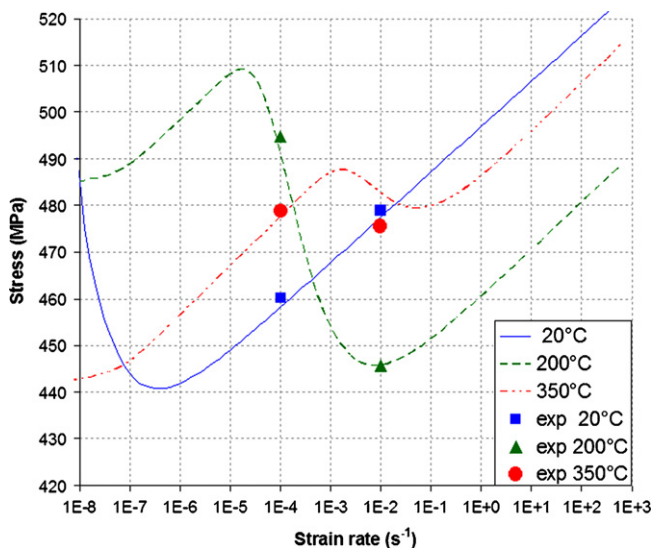


Fig. 4. Predicted flow stress at 6% strain versus strain rate for three temperatures. Comparison with experimental results obtained in tensile tests.

domain). For each temperature, an intermediate strain rate domain exists where the flow stress decreases when strain rate increases. This negative SRS behavior is characteristic of the domain of PLC instabilities.

#### 4.3. Numerical modeling of tensile tests

The set of temperature dependent parameters was obtained based on volume element simulations. As a result, no strain or strain rate localization was taken into account. In order to simulate these phenomena, the tensile specimens were modeled using the finite element code ZeBuLoN [23] including the KEMC constitutive equations. Small time steps are necessary to describe the very sharp serrations which characterize the PLC phenomenon. Global mechanical equilibrium is solved according to an implicit scheme by a quasi-Newton method using the elastic stiffness matrix. The number of time steps can thus be as large as 60,000 to compute 15% global strain. The number of time steps highly depends on the type of serrations. The computations were carried out within the updated small strain framework because no significant finite rotation effects were expected in the modeled tests.

To save computation time, 2D models were used. A comparison between 2D plane stress, 2D axisymmetric and full 3D computations was carried out. It turns out that the overall curves are similar in all three situations, even though the localization patterns may significantly differ. The type of serrations generally remains close (see Refs. [11,8]). In order to reduce the computation time, we chose the 2D model for the many simulations that are needed in the identification procedure, even though a more precise prediction of spatial distributions of mechanical variables, will probably require 3D simulations. Furthermore, the strain localizations do not probably save axisymmetry, so the plane stress assumption was chosen.

Accordingly, an equivalent rectangular plate specimen was modeled by a 2D mesh under plane stress conditions. The width of the plate was equal to the diameter of the cylindrical specimen to obtain the same maximal length of the bands. However, the influence of the width of the equivalent plate on the development of the localization bands was not investigated. Five hundred 8-node quadratic elements with reduced integration were used. The fillets with the head of the specimen were modeled explicitly (see the mesh in Fig. 5 or Fig. 6). These fillets are at the origin of the localization due to stress concentration. Nevertheless, to avoid the development of symmetric bands that are generally not observed experimentally, the triggering of the localization was enforced: a finite element presenting a lower yield stress than the others was placed at the bottom fillet. The yield stress was 0.84 of the rest of the material. Other types of defect were tested in Ref. [24] as geometrical defect, without much influence on the results.

The tension of the specimen was prescribed by the displacement of the upper nodes of the mesh at constant velocity, whereas the bottom nodes remain fixed in the loading direction. The gliding between the top and bottom edges is allowed. This condition modifies the geometry of the strain bands which are either inclined single planes or cross-shaped planes [24], but the load level or the serrations are not changed.

Figs. 5–7 show the simulated stress–strain curves given by the strain aging model using the final set of parameters. At 20 °C, at the beginning of plastic flow, the specimen exhibits first a localized plastic strain band (Fig. 5), associated with a corresponding yield drop observed on the tensile curve. Then the localized band extends and progressively covers the whole specimen. During this sequence, a Lüders plateau is observed on the tensile curve. In the simulations, the Lüders peak and plateau progressively vanish with increasing temperature, as observed experimentally. At 150 °C and 200 °C, PLC instabilities are observed on the stress versus strain curves (Fig. 6). For these simulations, the discontinuous yielding is

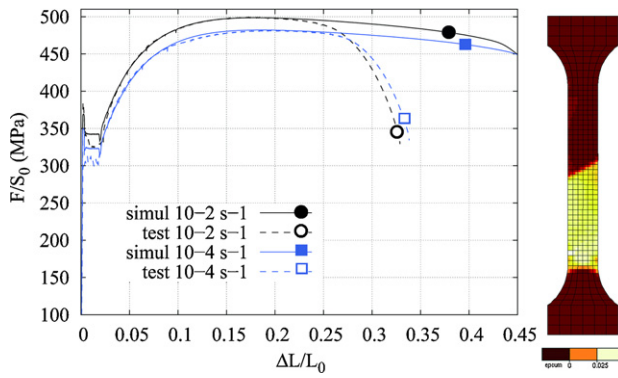


**Fig. 5.** Comparison between modeling of the tensile tests at 20 °C and experiments. Iso-contours of the cumulated equivalent plastic strain  $p$  during the Lüders (dark:  $p < 0$ ; white:  $p > 0.025$ ).

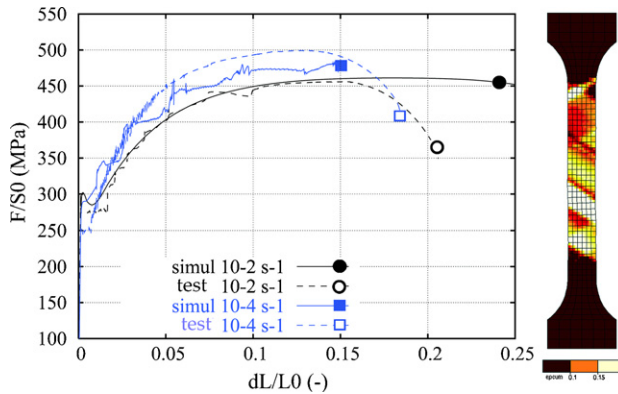


**Fig. 6.** Comparison between modeling of the tensile tests at 200 °C and experiments. Iso-contours of the cumulated equivalent plastic strain  $p$  during the PLC phenomenon (dark:  $p < 0.1$ ; white:  $p > 0.15$ ).

highlighted by localization bands of plastic strain rate appearing on the strain rate maps provided by the numerical model. At 350 °C, the strong apparent hardening is correctly predicted, as well as the weak strain rate sensitivity. However, for large strains, jerky flow is predicted at  $10^{-2} \text{ s}^{-1}$ , whereas experimental data do not show any jerky flow (Fig. 7).

The whole tensile test database was modeled. Even if necking cannot be correctly predicted by a 2D model for a cylindrical

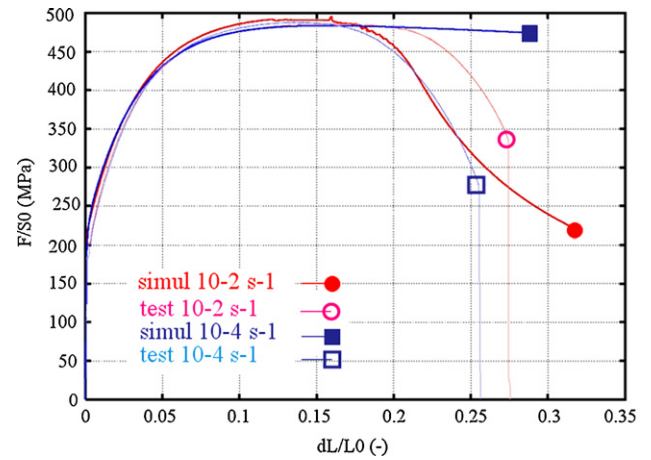


**Fig. 7.** Comparison between modeling of the tensile tests at 350 °C and experiments.

specimen, one can expect that the elongation before necking is essentially controlled by the behavior law. This uniform elongation predicted by the model was therefore compared to the experimental value in Fig. 8 for both strain rates. This figure shows that the predicted elongation before necking presents a drop in the temperature domain of dynamic strain aging as observed experimentally, with a shift towards higher temperatures for higher strain rates. The trend is correctly predicted, even though the detailed evolution, especially at  $10^{-4} \text{ s}^{-1}$  could be improved. It can be concluded that the temperature dependence of both hardening and strain rate sensitivity is correctly taken into account with the set of parameters identified, even though some detailed features remain imperfectly described.

### 5. Numerical modeling of fracture tests

#### 5.1. Finite element model

The strain aging model implemented in the finite element software accounts for most of the SSA and DSA features observed in tensile test. A further step consists in applying this model to examine the influence of strain aging on the tearing resistance. Simulations of fracture tests on CT specimen were thus performed with the KEMC constitutive model. A whole CT25 specimen (Fig. 9) was meshed with C2D8R elements (8-node quadratic elements with

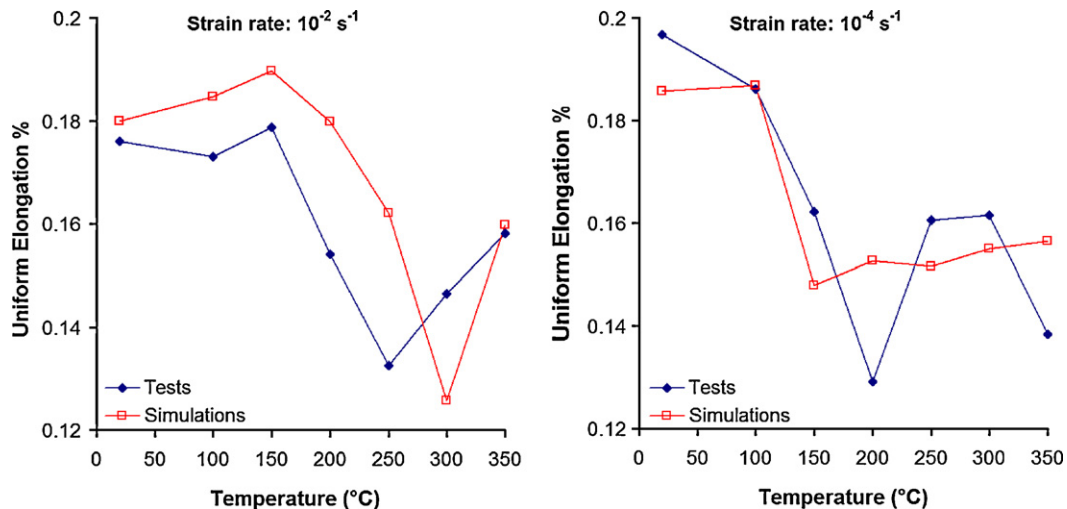


**Fig. 8.** Uniform elongation as function of temperature. Comparison between predicted and experimental values.

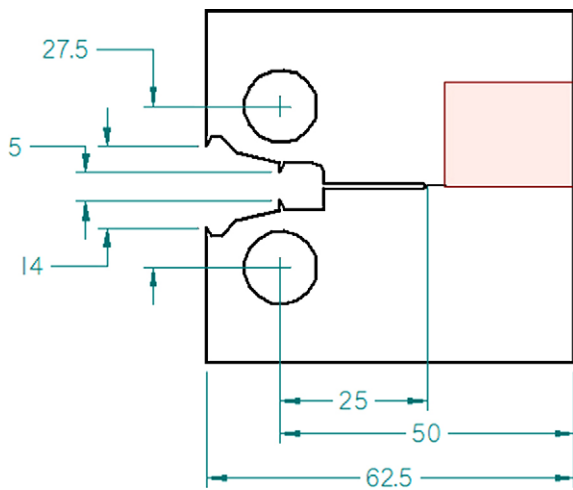


**Fig. 9.** Scheme of the section of the CT specimen (values in mm). The box indicated defines the zone observed in Figs. 10 and 12.

reduced integration) in the ZeBuLoN FE code. The mesh is composed of 10,585 nodes and 3480 elements, with a mesh refinement at the crack tip leading to a local mesh size of 0.1 mm. Both plane stress and plane strain conditions were tested.

The loading pins were modeled by element sets defined with a purely elastic behavior law. A displacement is prescribed at the pins with a constant velocity of 0.4 mm/min. The strain rate ahead of the crack tip was therefore estimated between  $10^{-4} \text{ s}^{-1}$  and  $10^{-2} \text{ s}^{-1}$  depending on the distance from the crack tip. Computations were carried out at two temperatures: Lüders behavior should be prominent at  $20^\circ\text{C}$  whereas SRS is negative at  $200^\circ\text{C}$ , for strain rates

ranging from  $10^{-4} \text{ s}^{-1}$  to  $10^{-2} \text{ s}^{-1}$ . The computations were analyzed for load line displacement up to 1.5 mm. At this value, no ductile tearing was observed in the experiments, which is consistent with the use of a constitutive model without damage law.

The results were compared to those obtained without taking into account strain aging in the constitutive equations ( $P_1 = 0$ ).

## 5.2. SSA induced localization at the crack tip at $20^\circ\text{C}$

Fig. 10 shows the plastic zones at the crack tip of a CT specimen computed with and without the use of the strain aging constitutive equations. The comparison is done under plane stress and plane strain conditions. Post-processing maps are extracted from the part of the specimen situated between the crack tip and the back-side of the specimen, including the edge, at 1.5 mm of crack opening displacement.

The plastic zones obtained without SSA (top of Fig. 10) exhibit the classical shape around the crack tip: under plane stress conditions, the plastic zone is circular, and under plane strain, the plastic zone follows the usual “butterfly wing” shape. Plastic strains smaller than 3% are also observed at the back-side due to the global bending of the specimen. We can note that, under plane strain conditions, the two plastic strain zones at the crack tip and at the specimen free edge tend to join together.

A larger plastic zone size than that of the classical one, is observed at  $20^\circ\text{C}$  (bottom of Fig. 10) when SSA is taken into account at  $20^\circ\text{C}$ . Under plane stress conditions, plastic flow localizes along bands parallel to the crack growth direction. Under plane strain conditions, localized bands are first observed perpendicularly to the crack plane and then the plastic zone branches into two curved paths merging at the back-side of the specimen. In both cases, we note a large plasticity area at the back-side of the specimen.

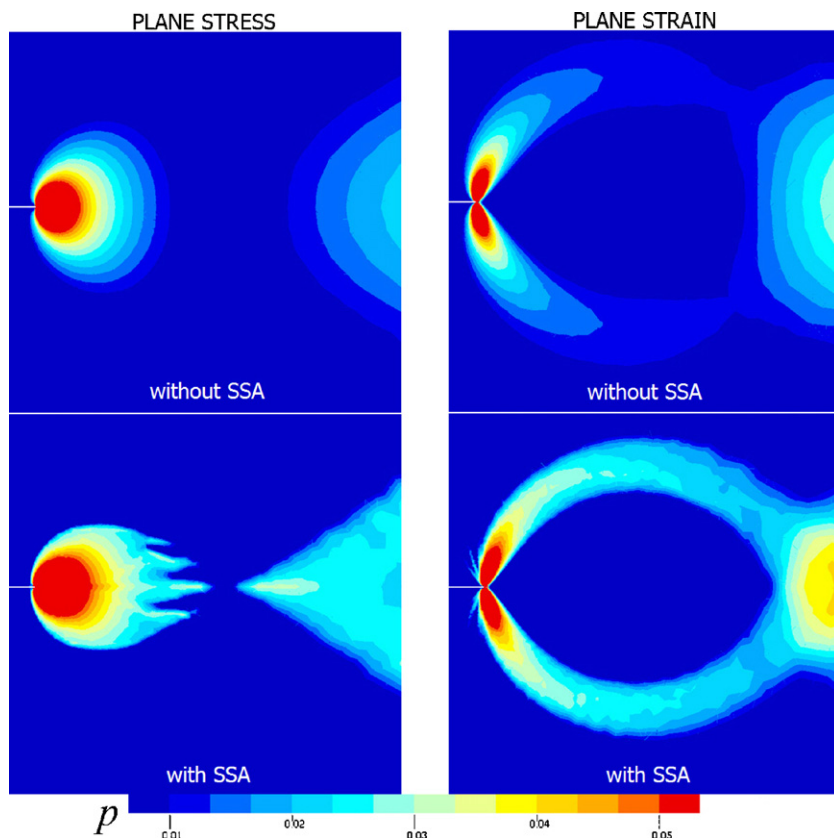


**Fig. 10.** Iso-contours of cumulated equivalent plastic strain  $p$  at the crack tip for a load line displacement of 1.5 mm (half box defined in Fig. 9) for plane stress (left) and plane strain (right). Prediction for  $20^\circ\text{C}$  with  $P_1 = 0$  (without static strain aging) and with the parameter set as identified in Section 4 (with static strain aging).

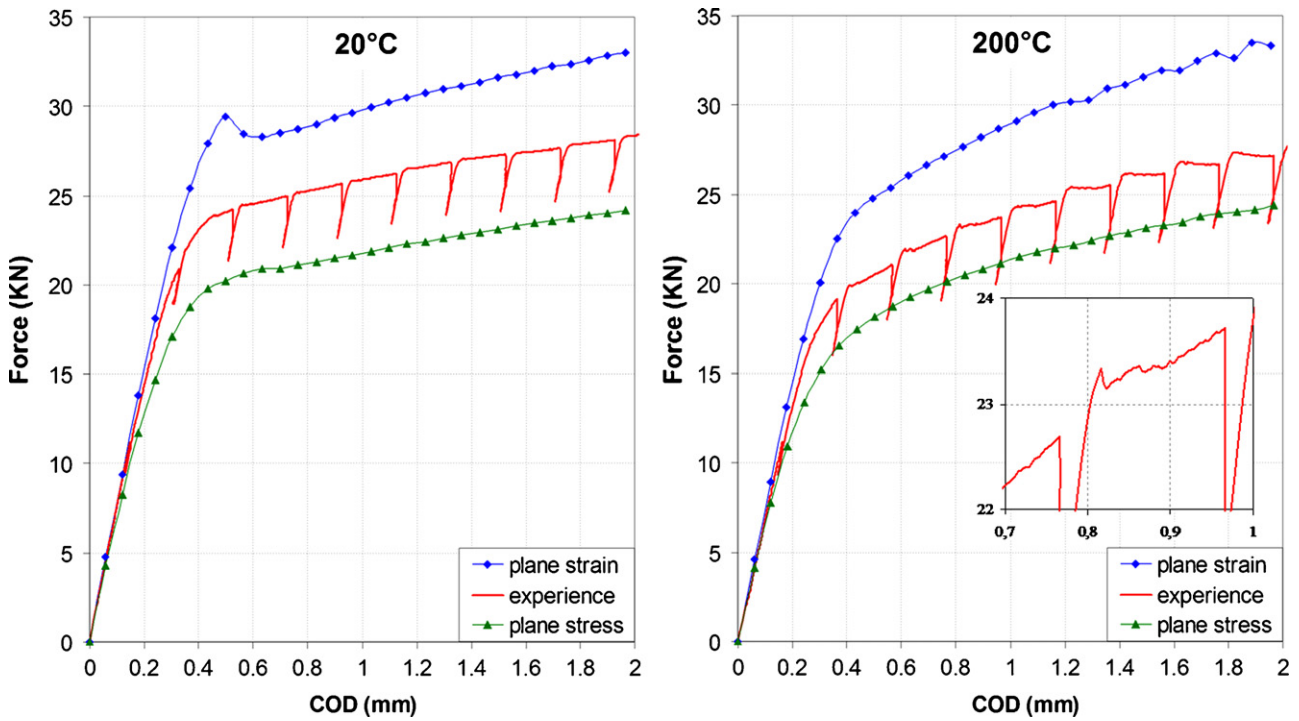


Fig. 11. Load versus the crack opening displacement at 20 °C (left) and at 200 °C (right). Comparison between the finite element model and experiment.

The experimental load versus crack opening displacement curve is located between the predicted curves obtained with the KEMC model under plane strain and plane stress conditions (Fig. 11). This result confirms that the material parameters allow a correct modeling of the behavior of the material, although in side-grooved specimens, the experimental situation should be closer to plane strain conditions. The plane strain curve exhibits a load peak that is not observed on the plane stress one.

5.3. DSA induced localization at the crack tip at 200 °C

Computations were also performed at 200 °C under plane strain and plane stress. The load versus load line displacement curve for each simulation plotted in Fig. 11 shows that the experimental curve lies between plane stress and plane strain modeling as expected. The unloading sequences were not simulated so that the numerical

curve does not display the slight peaks observed at 200 °C on the experimental curve after each reloading.

Fig. 12 presents the corresponding plastic strain rate maps. Post-processing maps are extracted at 0.65 mm load line opening displacement. Taking DSA into account at 200 °C does not induce noticeable variations of the plastic zone size compared to the classical one. Nevertheless, plastic flow is found to localize in thin bands. In both cases (plane stress and plane strain), plastic strain rate localizes in bands at the early stage of crack tip opening. The morphology of these bands strongly depends on the plane stress or plane strain condition. Under plane stress conditions, “flashing” plastic strain rate bands appear and disappear for increasing loading. The bands remain always inside the circular plastic zone found when DSA is neglected. They are oriented in the crack propagation direction. Under plane strain conditions, the bands are contained in the “butterfly wing”-shape of the plastic zone obtained in the absence of

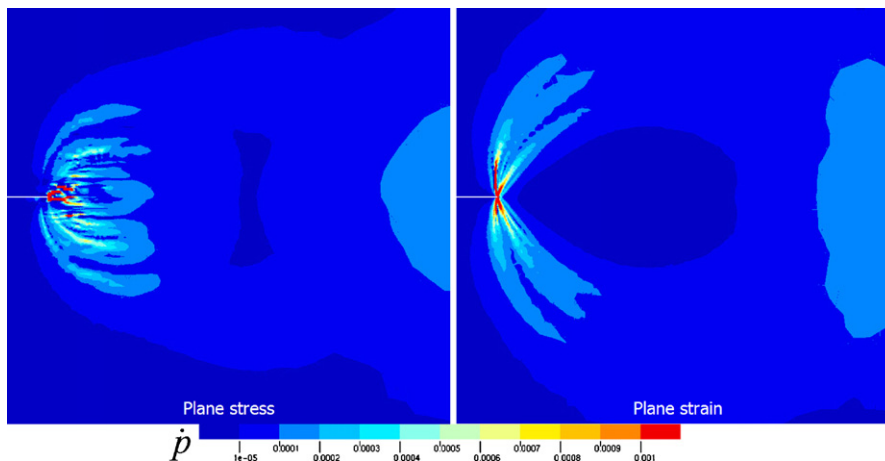


Fig. 12. Iso-contours of equivalent plastic strain rate  $\dot{p}$  at the crack tip for a load line displacement of 0.65 mm for plane stress (left) and plane strain (right). Temperature is 200 °C.

DSA. They are oriented perpendicularly to the crack propagation plane.

## 6. Discussion

The mechanical behavior in tension is correctly described by the proposed set of material parameters. The temperature domain of negative strain rate sensitivity is captured by the model. The flow stresses as well as the uniform elongation are predicted for the seven temperatures and the two strain rates. However, the jerky flow observed experimentally for tensile tests at 200 °C and a strain rate of  $10^{-4} \text{ s}^{-1}$ , are not adequately described by the numerical model. A further, more accurate identification of the parameters of the constitutive equations, based on an extended database, could improve the accuracy of the results. This would require new information, such as the strain amplitude inside the localized bands. It must be noted that the experimental techniques, optical pyrometry and extensometry, usually applied to study DSA at room temperature in aluminum alloys [25] are difficult to transfer to DSA in steels which occurs at much higher temperature. Finally, considering the number of closely related parameters to be identified, the question of establishing a well-defined identification procedure is raised.

Nevertheless, the FE simulations of the tensile tests in the presence of SSA and DSA give realistic descriptions of the various stress–strain curves measured experimentally in these temperature and strain rate domains. Plastic instabilities associated with Lüders and Portevin–Le Chatelier phenomena are both predicted in the expected temperature range, even though the stress levels and the detailed serrations are not yet exactly the same as the experimental ones.

Another interesting result is the non-monotonic evolution of  $Q$  that came out of the identification process. The necessity to increase the strain hardening parameter  $Q$  suggests a shortcoming of the KEMC model. In the constitutive equations, classical strain hardening is defined independently from strain aging. Indeed, while dislocations are pinned during the aging process, the creation of new dislocations is needed. Furthermore, the difficulties encountered when fitting the  $P_1$  value over the whole temperature range seem to indicate that the hypothesis considering a single pinning kinetics for SSA and DSA is probably too crude and should be re-examined. Some other simplifications, such as the plastic strain and temperature independent  $\omega$  value, that indirectly drives the intensity of the pinning process through the aging time  $t_a$ , should also be modified.

The mesh sensitivity of the numerical solution was investigated by testing three different finite-element meshes: two regular meshes with 500 or 2000 elements and a random free mesh with varying mesh size of 3500 elements. The numerical results are practically mesh size independent. It can be concluded that mesh effects are not predominant for the apparition of localization bands. For Lüders band simulation, the influence of mesh size on the morphology of the plateau on the simulated stress–strain curves is negligible [24]. Nevertheless, changing the mesh size can induce modifications of the width of localized Portevin–Le Chatelier bands: a finer mesh leads to smaller band width. But mesh dependency is limited to the thickness of the PLC bands and the strain rate inside, whereas the plastic strain brought by one band is mesh independent. As a result, the overall behavior and deformation pattern can be regarded as practically mesh insensitive. The reason lies in the positive rate dependency that always follows the negative SRS regime for higher strain rates and thus stabilizes the material response.

The FE simulations of fracture tests on CT specimens, taking strain aging into account, display plastic strain localization at the crack tip, associated with SSA at 20 °C and DSA at 200 °C. The DSA band morphology, simulated under plane stress conditions, is in

agreement with the results of previous studies carried out with other material parameters [26]. The shape of the DSA bands simulated under plane stress conditions is also in accordance with the experimental observations performed on Al–Li during *in situ* testing of plate CT specimens, where DSA is active [27]. Load peaks at SSA temperatures and serrations at DSA temperatures also correspond to the experimental load versus load line displacement curves (Fig. 11). Even though the details of the morphology of bands should depend on the material (width of the bands as well as the strain intensity in the localizations), the shape of the plastic zone is a mechanical consequence of the negative strain rate sensitivity which is probably independent of the material type. Since the plastic zone characteristic of DSA is correctly described by the model, and the load versus displacement curve lies between the 2D bounds, we can consider that the model identified from tensile tests also provides a correct estimation of the local mechanical fields at the crack tip in the presence of strain aging. Quantitative strain field measurements are necessary to confirm this point.

The SSA and DSA simulations of plastic strain localization at the crack tip will offer the possibility of investigating more precisely, in subsequent studies, the role of plastic strain instabilities in the reduction of fracture toughness. If strain localizes, it is probable that damage localizes too, so that the question of volume damage or surface damage arises. Indeed, localization of mechanical fields due to SSA/DSA could favor crack initiation and accelerate fracture. It is now a challenge to couple this mechanical behavior modeling of strain aging effects, with ductile damage models for the prediction of crack propagation resistance [28].

## 7. Conclusion

Strain aging occurs in steels containing interstitial elements in solid solution such as carbon or nitrogen, which segregate to dislocations thus inducing dislocation pinning. This interaction induces the Lüders phenomenon as well as the PLC phenomenon associated with a drop in ductility and in tearing strength. For the prediction of these mechanical properties' evolution, we used the KEMC model which takes the physical origin of strain aging into account, through an internal variable, the aging time.

This work mainly aimed to identify the parameters of this model in the 20–350 °C temperature range for quasi-static loadings from a tensile test database. This was a difficult task because simulations on volume element are not able to describe the spatial distribution of the variables. Full FE simulations are therefore required for the identification of the parameters of the model. This study raises the question of establishing a robust identification procedure for this model, particularly when temperature varies. Evolution laws of the parameters with temperature could be proposed from the results of this work. The temperature dependence is quasi-monotonic for all the parameters, except for the strain hardening parameter  $Q$ : one important result of this study is the predicted extra-hardening due to DSA at intermediate temperatures. The simultaneous description of SSA and DSA effects with a single internal variable  $t_a$  was possible but it has some limitations. The two last points should be corrected by a new formulation of the model that is under development.

The FE model of the tensile test gives a good description of the various stress–strain curves measured experimentally in these temperature and strain rate domains. Plastic instabilities are predicted in the expected temperature range, even though the stress levels and the detailed serrations are not yet exactly the same as the experimental ones. The validation should further be done with 3D computations. The prediction of the fracture tests on CT specimens is accurate too. The strain aging model, which has been identified from the tensile tests, also yields an estimation of the local mechanical fields at the crack tip in the presence of SSA or DSA. A further

step for this study will be to compare classical variables, such as stress triaxiality, which drive ductile damage calculated with and without strain aging.

### Acknowledgments

Financial support of EDF Company and fruitful discussions with Patrick Le Delliou are greatly acknowledged. The authors would like to express their thanks to Jean-Loup Strudel for his contribution to the physical interpretation of the results.

### References

- [1] L.P. Kubin, Y. Estrin, *Acta Metall.* 33 (1985) 397–407.
- [2] K.W. Lee, S.K. Kim, K.T. Kim, S.I. Hong, *J. Nucl. Mater.* 295 (2001) 21–26.
- [3] D. Wagner, J.C. Moreno, C. Prioul, *J. Nucl. Mater.* 300 (2002) 178–191.
- [4] M. Srinivas, G. Malakondaiah, K.L. Murty, P.R. Rao, *Scripta Metall. Mater.* 25 (1991) 2585–2588.
- [5] M. Srinivas, G. Malakondaiah, P.R. Rao, *Acta Metall.* 41 (1993) 1301–1312.
- [6] J.D. Baird, *Iron Steel* 3 (1963) 183–196.
- [7] H. Tsukahara, T. Jung, *Mater. Sci. Eng. A248* (1998) 304–308.
- [8] A. Benallal, T. Berstad, T. Børvik, A.H. Clausen, O.S. Hopperstad, *Eur. J. Mech. A25* (2006) 397–424.
- [9] Y. Estrin, P.G. McCormick, *Acta Met. Mater.* 39 (1991) 2977–2983.
- [10] P.G. McCormick, C.P. Ling, *Acta Met. Mater.* 43 (1995) 1969–1977.
- [11] S. Zhang, P.G. McCormick, Y. Estrin, *Acta Mater.* 49 (2001) 1087–1094.
- [12] S. Graff, S. Forest, J.L. Strudel, C. Prioul, P. Pilvin, J.L. Béchade, *Mater. Sci. Eng. A387* (2004) 181–185.
- [13] D. Wagner, J.C. Moreno, C. Prioul, *J. Nucl. Mater.* 252 (1998) 257–265.
- [14] D. Wagner, J.C. Moreno, C. Prioul, *Rev. Métall.* 97 (2000) 1481–1500.
- [15] K.C. Kim, J.T. Kim, J.I. Suk, U.H. Sung, H.K. Kwon, *Nucl. Eng. Des.* 228 (2004) 151–159.
- [16] A. Nadai, *Theory of Flow and Fracture of Solids*, vol. 1, McGraw-Hill Company, 1950, p. 298.
- [17] Y. Estrin, L.P. Kubin, in: H. Muhlhaus (Ed.), *Continuum Models for Materials with Microstructure*, Wiley, 1995, pp. 395–450.
- [18] P.G. McCormick, *Acta Metall.* 36 (1988) 3061–3067.
- [19] P. Pilvin, in: C. Oytana, et al. (Eds.), *Proc. of Mecamat Conference on “inelastic behaviour of solids”*, 1988, p. p. 155 (Besançon, France).
- [20] S. Graff, H. Dierke, S. Forest, H. Neuhäuser, J.L. Strudel, *Philos. Mag.* 88 (2008) 3389–3414, doi:10.1080/14786430802108472.
- [21] M. Mazière, J. Besson, S. Forest, B. Tanguy, H. Chalons, F. Vogel, *Eur. J. Comput. Mech.* 17 (2008) 761–772, doi:10.3166/remn.17.761-772.
- [22] O.S. Hopperstad, T. Børvik, T. Berstad, O.G. Lademo, A. Benallal, *Modell. Simul. Mater. Sci. Eng.* 15 (2007) 747–772.
- [23] Z-set package, <http://www.nwnumerics.com>, <http://www.mat.ensmp.fr>, 1996.
- [24] J. Belotteau, C. Berdin, S. Forest, A. Parrot, C. Prioul, 16th European Conference on Fracture, Alexandroupolis, Greece, 2006.
- [25] N. Ranc, D. Wagner, *Mater. Sci. Eng. A474* (2008) 188–196.
- [26] S. Graff, S. Forest, J.L. Strudel, C. Prioul, P. Pilvin, J.L. Béchade, *Scripta Mater.* 52 (2005) 1181–1186.
- [27] D. Delafosse, G. Lapasset, L.P. Kubin, *Scripta Metall. Mater.* 29 (1993) 1379–1384.
- [28] A. Needleman, V. Tvergaard, *J. Mech. Phys. Sol.* 35 (1987) 151–183.